

Digital crossed-beam holography for *in situ* imaging of atmospheric ice particles

S M F Raupach¹, H J Vössing¹, J Curtius¹ and S Borrmann^{1,2}

¹ Institut für Physik der Atmosphäre, Johannes Gutenberg-Universität Mainz, D-55099 Mainz, Germany

² Max-Planck-Institut für Chemie, Joh.-Joachim-Becher-Weg 27, D-55020 Mainz, Germany

E-mail: raupa@uni-mainz.de

Received 13 April 2006, accepted for publication 7 July 2006

Published 25 July 2006

Online at stacks.iop.org/JOptA/8/796

Abstract

A ground-based outdoor digital-holographic particle imaging system is described, which uses a nanosecond pulsed laser and CMOS cameras in an inline set-up to image atmospheric particles *in situ*. Sharp images can be digitally reconstructed from the diffraction images. The system uses two crossed beam paths, yielding a total sample volume of roughly 9.9 cm³ where particles with a spatial extent orthogonal to the beam path between 10 μm and several millimetres can be imaged. The set-up allows for two views of objects within an atmospheric cross volume of about 0.3 cm³, defined by the intersecting beams. It is demonstrated how this can be used for an accurate determination of three-dimensional distance relationships within the cross volume, in addition to determining sizes and shapes of moving airborne particles. To this end, results from a field test on the High Altitude Research Station Jungfraujoch in the Alps are shown as examples.

Keywords: digital holography, crossed beam set-up, atmospheric sciences, nanosecond pulsed laser, CMOS camera, cloud element imaging, hydrometeor size

1. Introduction

In atmospheric sciences, pulsed holography has long been regarded as a potentially versatile tool to determine microphysical quantities like size, shape and distance distributions of moving airborne particles, such as droplets or ice crystals ('hydrometeors') in clouds [2, 3, 6]. These quantities are of interest e.g. in investigations of cloud microphysics and radiative effects of cloud particles, but also when trying to determine surface area and volume of atmospheric particles to understand their role in atmospheric chemistry or to understand processes like riming or snow formation.

In allowing us to record a three dimensional snapshot of an atmospheric sample volume, this technique has advantages over non-holographic imaging devices traditionally used in this field [19]. These devices only within a small and size-dependent depth-of-field yield accurate two dimensional projections of objects in the observed volume [21]. Non-imaging optical measurements based on the intensity of

scattered light according to the Mie theory, also commonly used in atmospheric sciences, are of limited use for non-spherical particles considerably larger than the wavelength of the probing light, where deviations from the assumed spherical shape have considerable effects. There have been efforts to correct for these effects [25], but these corrections are only valid for particles smaller than 16 μm, where certain conditions have to be met. Also, for large aspherical particles, such as ice crystals, the concept of describing the particles' size by assigning a single radius to them may only be suited for special applications.

Although there have been several efforts to employ the holographic technique in this respect [2–4, 9, 10, 12], traditional analogue holography using photographic emulsions and optical reconstruction, so far has not become a standard tool. This was partly caused by the mechanical and chemical requirements for exposure and development of the photographic emulsion and by the need to have an expensive, rather large and involved high-energy laser system in the case of pulsed holography, but most severely by the laborious

analysis of analogue holograms [9, 10, 12, 20], which despite several automatization efforts [8, 18] rendered data processing extremely time consuming and operator intensive. With the arrival of digital imaging devices and increasing computer power, digital holography became feasible [5, 13], where digital cameras are used instead of photo-chemical films. This relaxes the requirements for the intensity of the laser light, as typical CCD and CMOS imaging chips are more sensitive to light than fine-grained holographic film material. Also, digital recording devices seem not to be subject to an effect comparable to the so-called ‘reciprocity failure’ of photo-chemical materials [7], i.e. an over-proportional increase in intensity required for proper exposure with extremely short light pulses.

In contrast to analogue holography, where reconstruction is done optically with a special system set up in the laboratory, numerical reconstruction by a computer delivers digital images, ready for further analysis. Thus the digital-holographic technique was met with renewed interest [14], and its general versatility for measurements of atmospheric particles was demonstrated with air-borne digital holographic systems [19, 29].

As digital imaging devices with typical pixel sizes on the order of a few microns are rather coarse relative to the wavelength of visible light, digital holography is essentially restricted to the inline set-up described in detail elsewhere [1, 29], where light source, object, and imaging device basically are on one axis. In the ‘diffractometric’ set-up commonly used, where light source and imaging device are on opposite sides of the object, mainly the silhouettes of the particles are reconstructed [29], although in objects such as ice crystals additional structures can also be discerned [19]. However, when aiming at measuring three-dimensional distance relationships, e.g. to accurately determine inter-particle distances or particle sizes, the inline set-up has certain drawbacks. In particular, determining the depth position, i.e. the position along the optical axis, is challenging in single-beam inline set-ups due to a rather large and typically particle-size dependent depth of field (see e.g. [15, 21]). To improve depth resolution, analogue inline–offline ‘hybrid’ set-ups have been suggested, which however involve filtering of the zero-order scattered light during recording of the hologram [15, 16].

In atmospheric sciences also an estimate of the particles’ volume, as well as of the surface area, is of special interest: these quantities in combination with measured concentrations of gaseous and particulate chemical species [22, 27, 31] allow for an estimate of the role of heterogenous chemistry and uptake of chemical species from the gas phase. These effects are of crucial importance e.g. when studying the chemistry of stratospheric ozone depletion.

Determining the exact surface area by optical methods requires knowledge of or assumptions on the sub-resolution roughness of the surfaces and therefore presents special challenges. However, for non-spherical particles such as ice crystals, even determining the particles’ volume from a single view of the particles’ silhouettes is not straightforward. Therefore new and improved *in situ* instrumentation with non-destructive sampling capabilities for airborne particles such as droplets, ice crystals or other hydrometeors is desirable.

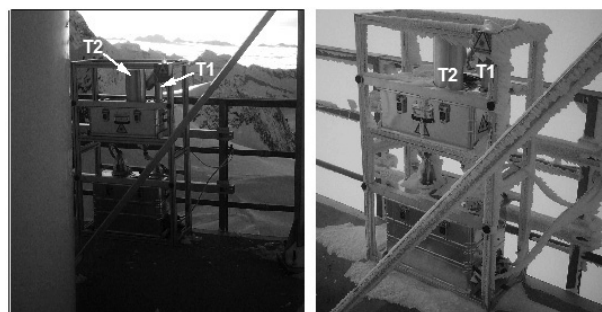


Figure 1. The digital holographic imaging system on the High Altitude Research Station Jungfrauoch shortly after its set-up on 26 February 2006 (left), and some days later after considerable riming from cloud exposure (right). The lower box contains the laser and camera control and data-storage unit, the upper box the laser, cameras and optics. On top of the laser box the two camera towers, labelled T₁ and T₂ and being of slightly different designs, can be seen. They stand at right angles towards each other.

In this paper, we describe the prototype of a cost effective outdoor, ground-based digital holographic system for imaging atmospheric particles *in situ*, that at least partly overcomes the limitations of inline holography by using a crossed-beam set-up. We show as examples first results from a field test at the High Altitude Research Station Jungfrauoch in the Swiss Alps in February and March 2006.

2. Description of the instrument

In the current set-up, the instrument as shown in figure 1 consists of two waterproof, thermally controlled aluminium boxes sized 0.60 m × 0.40 m × 0.25 m and 0.60 m × 0.40 m × 0.41 m. The first contains the laser and camera control as well as the data storage unit; the second contains the laser-optical and imaging unit. The boxes are mounted in an aluminium frame, yielding a total height of the instrument of 1.27 m.

The laser unit consists of a passively *Q*-switched, frequency-doubled Nd:YAG laserhead (CryLas), specified for a temperature range between +10 and +35 °C. It delivers pulses with an average energy of 10 μJ and of approximately 1 ns duration as specified by the manufacturer. It emits radiation at a wavelength of 532 nm and operates in the TEM₀₀ mode.

The laser beam is expanded and collimated using a set of two anti-reflection coated lenses (see figure 2), an aspherical lens with a focal length of 4 mm (L₁), and a plano-convex lens with a focal length of 75 mm (L₂), respectively. Following expansion and collimation, the beam is transmitted through a non-polarizing 50/50-beamsplitter cube (BS), where the beam is split up into two beams travelling at an angle of 90°. Using mirrors which reflect incoming light at an angle of 90°, where the mirrors are turnable about the optical axis, the laser beams are sent upwards in a 45° angle with respect to the plane of the optical components (see figure 2), such that they cross each other above the lid of the box, defining a cross volume where they intersect at an angle of 60° and continue each towards its camera (see figure 3).

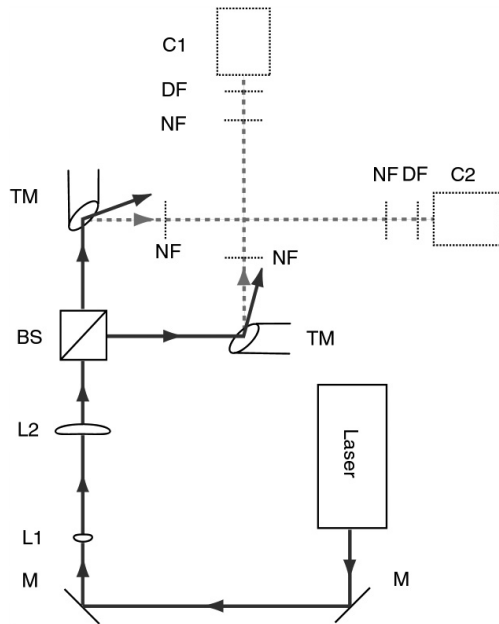


Figure 2. A schematic top view of the optics set-up (not to scale). The beam path (dark grey) is folded using two mirrors (M). The laser beam is expanded and collimated by a set of two convex lenses with focal lengths of 4 mm (L1) and 75 mm (L2), respectively. Using a non-polarizing 50/50 beam-splitter cube (BS), the laser beam is split into two travelling at right angles. Each beam is sent upwards at an angle of 45° with respect to the plane of the drawing by turnable mirrors (TM). For clarity the tilted beam path, the neutral density filters (NF), the dichroic filters (DF) and the cameras (C1, C2) are depicted as projections onto the plane of the drawing (dashed lines; see also figure 3).

Each beam's intensity is diminished by neutral density filters (NF) serving at the same time as exit/entrance windows. They have a total optical density of 1.3 (0.3 for the exit windows and 1.0 for the entrance windows) and are combined with a green dichroic bandpass filter (DF) immediately in front of the camera (C1, C2) to filter out unwanted background light.

The cameras are housed in heated, waterproof 'camera towers' of slightly different design. Each tower with camera can be dismantled separately. The camera towers stand at right angles towards each other, and the cameras are inclined towards the lid of the laser-optical box by an angle of $\gamma = 45^\circ$ (see figure 3). For design reasons, the camera in tower T₂ (figure 1) is turned upside down with respect to the camera in the other tower. All images shown in this paper which were taken by the camera in tower T₂ have been rotated back accordingly.

Tower T₁ is mounted such that for alignment purposes it can be turned about its axis orthogonal to the lid before being fixed.

The cameras used are monochrome 1.3 Megapixel Firewire CMOS cameras A622f (Basler), which instead of the commonly used CCD sensor [13, 19, 29] contain a CMOS chip of 1024×1280 pixels, where each pixel is sized $6.7 \mu\text{m} \times 6.7 \mu\text{m}$. The cameras deliver a 'Trigger Ready' and 'Picture is being taken' signal that is used to trigger the laser in dependence on the operational status of the cameras. Out of the 1024×1280 pixels only 1024×1024 are read out in our case.

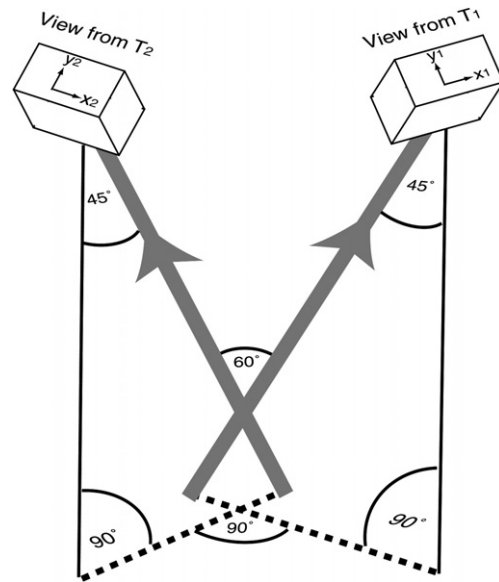


Figure 3. A schematic view of the beam path (not to scale). Shown is a sketch of the crossing laser beam paths (grey). The beams intersect at an angle of 60° . The angle of 90° between the projections of the beam paths onto the plane of the lid corresponds to θ , the angles labelled 45° correspond to $90^\circ - \gamma$. For clarity of the drawing not shown are the neutral density filters with an optical density of 1.0, which serve as entrance windows, and the dichroic bandpass filters.

The distances between the exit and the entrance windows are roughly 8.8 and 12.3 cm respectively, yielding a total sample volume of about 9.9 cm^3 when multiplied by the area of the sensor. Setting up the system using crossed beams and two cameras instead of using a single beam and camera [19, 29] not only enlarges the observed volume, but also makes it possible to gain two views of objects within a cross volume of about 0.3 cm^3 .

To ensure appropriate thermal conditions, the baseplate of the optics and the laser head is thermally insulated from the rest of the box including the camera towers, and is heated by a maximum of 400 W, where different bimetal switches control the heating power. Tests at the Mainz walk-in cold chamber using 300 W of heating power confirmed that at an ambient temperature of -25°C and little convection the temperature at the position of the laserhead would not drop below $+16^\circ\text{C}$. As a safety margin, another 100 W of heating power were added prior to the field test. The control box in contrast is heated by 200 W only, as there also the computer itself contributes to the heating.

The control and data storage unit of the digital holographic imaging system consists of an ordinary PC (Shuttle XPC SB95P2), an electronic pulse stabilizer and a laser control unit.

The PC's task is to trigger the laser control in dependence on the status of the cameras, to read out the camera chips and to store the images. The cameras' operational status is read out using the PC's parallel port, which is also used to send the trigger signal to the laser control unit. The cameras are not running freely but are operated in a 'one-shot' mode, where the acquisition of each image is triggered by the PC. The images are transmitted by the cameras via two IEEE1394a-connections sharing the PC's IEEE1394a bus. The PC has a

storage capacity of 0.5 Tbyte on its hard disk, corresponding to a storage capacity of about 250 000 uncompressed double images.

During tests, we experienced problems with a varying length of the trigger signal delivered by the PC, which led to undesired behaviour of the laser system. Therefore, the PC-trigger signal is fed into an electronic trigger stabilizer, which in turn sends out stable trigger signals of about 1 ms duration to the control unit. The laser control then triggers the laser head and also monitors its status. The control and storage is done using custom C++-routines.

Via an RJ45-connection, an external PC can be connected to the control PC to download data or change camera or laser settings or the settings of the control software. Using a USB connection, an antenna can be plugged in alternatively to communicate via a wireless network connection. The only required external connection is a power cord delivering a voltage of 230 V AC and a power of 1 kW.

3. Field deployment at the High Altitude Research Station Jungfraujoch

The High Altitude Research Station Jungfraujoch is located in the Swiss Alps, next to Mt Jungfrau, Mt Mönch and Mt Eiger, at an altitude of roughly 3580 m above sea-level. Here an international field campaign termed ‘Cloud and Aerosol Characterization Experiment (CLACE) 5’ took place in February and March 2006. The purpose of the campaign was the investigation of ice nuclei and atmospheric ice particles in mixed phase clouds, that contain ice particles and supercooled droplets. In our case, the campaign served as a first field test of the instrument shown in figure 1. The digital-holographic particle imaging system was set up and running from 26 February to 21 March 2006. The environmental conditions experienced during that time covered temperatures from -1.3°C down to -29.6°C , with average air speeds (averaged over 10 min) of up to 120 km h^{-1} and peak air speeds of up to 175 km h^{-1} , and clear, sunny days as well as days with dense clouds and heavy snowfall. From 26 February to 2 March the instrument was run in a two-beam set-up; afterwards it was run in a one-beam set-up, as a piece of the optics not fixed properly had moved due to wind induced mechanical vibrations.

As each two-beam picture corresponds to a file size of 2Mbyte, the instrument was not run constantly at its highest frame rate of about 12 double pictures s^{-1} , corresponding to a data rate of 24 Mbyte s^{-1} ; instead the frame rate was varied and usually was on the order of several pictures per minute to save disk space. Note that the maximum frame rate for two cameras was limited by sharing the bandwidth of roughly 400 Mbit s^{-1} of the 1394a bus and the software operations, not by the cameras themselves, which individually could be operated at approximately twice that rate. In total, several tens of Gigabytes of uncompressed image data were acquired during the campaign, corresponding to several tens of thousands of holograms. As the frame rate was set to a constant value, the ‘yield’ of the instrument, i.e. the proportion of empty holograms to holograms capturing atmospheric objects, varied with the actual density of atmospheric particles.

The combination of neutral density filters and a bandpass filter for each beam proved to be sufficient to avoid spurious effects of the ambient sunlight, which can be rather intense at an altitude of 3500 m. Sunlight directly reflected off the optical box’s lid into the camera, however, was initially a problem, but covering the aluminium with strongly absorbing material solved this.

The rugged heating system controlled solely by bimetal switches kept the temperature in a range appropriate for all components to work.

4. Examples of numerically reconstructed holograms and their interpretation in the cross-view

4.1. Numerical reconstruction

The reconstruction method of digital holograms is described in detail elsewhere (see e.g. [13, 29, 30]), so only a brief overview is given here.

Numerical reconstruction is done using the Kirchhoff–Sommerfeld diffraction formula (also known as the Rayleigh–Sommerfeld formula) [7, 30]:

$$E_{\text{rec}}(\xi, \eta, z) = i/\lambda \int_{-\infty}^{+\infty} \int_{-\infty}^{+\infty} f_{\text{obliq}} H(x, y) E_{\text{ref}} \times \frac{\exp(-i2\pi R/\lambda)}{R} dx dy, \quad (1)$$

where E_{rec} is the amplitude of the reconstructed scalar wavefield in the ξ, η -plane at a distance z from the plane of the hologram, $H(x, y)$ is the intensity distribution in the plane of the hologram (i.e. the image taken by the camera, which in our case would be an image with eight-bit resolution), and E_{ref} is the amplitude of the scalar reference wavefield to be ‘diffracted’ by the holographic pattern $H(x, y)$. In our case, the reference wavefield is chosen to be a planar wave and its amplitude set equal to unity.

The ‘obliquity factor’ f_{obliq} derived by Sommerfeld is $f_{\text{obliq}} = z/R$; it is usually denoted as $\cos \Theta$. However, for many digital holographic set-ups the factor can be regarded as a constant with $f_{\text{obliq}} \approx 1$. For the reconstructions of the holograms presented in this paper it is treated as a constant.

The radius R is given by $R = [(x - \xi)^2 + (y - \eta)^2 + z^2]^{\frac{1}{2}}$, with z being the distance between the holographic and the reconstructed plane as before. Thus, the diffraction formula essentially is a convolution of the holographic diffraction pattern and a point source of light, delivering the complex amplitude of the light field in a plane at a distance z from the plane of the hologram. The numerical reconstruction of the volume is therefore not done at once, but by varying z it is done plane by plane.

The numerical computation of the convolution is sped up considerably by taking advantage of the Convolution Theorem of the theory of Fourier transforms. It states that the Fourier transform of a convolution of two functions is equivalent to the product of the individual Fourier transforms [24, 30]. Thus a convolution can be computed by multiplying the Fourier transforms of the individual functions with each other and applying an inverse Fourier transform to the result. Hence the usual reconstruction procedure, also followed in our case, is the following:

- (i) Fourier transforming the digital hologram, where the Fourier transform is implemented using an FFT algorithm;
- (ii) multiplying the transformed hologram with the Fourier transform of the convolution function for the desired distance z ;
- (iii) applying an inverse Fourier transform to the product, again utilizing an FFT algorithm;
- (iv) taking the modulus squared of the resulting complex amplitude as a function of (x, y) to get an intensity image.

In contrast to the procedure described in [29] the hologram is not greyscale-inversed prior to reconstruction; instead, holograms are generally normalized through division by other holograms, typically holograms taken immediately before or after the one to be normalized. This procedure, when applied at small particle number densities, has several advantages: It improves the image quality considerably by diminishing variations in the common background, thereby relaxing the demands for a clean beam profile, and in most cases it also renders a rescaling of the image intensities to emphasize the reconstructed objects [29] unnecessary, if the holograms used for normalization are ‘empty’, i.e. contain no diffraction patterns caused by particles. Alternatively, combining two holograms in this way, where both contain diffraction patterns caused by objects in the volume, can with some caution in principle be used to enhance the speed of reconstruction by a factor of two. This is because the objects in the respective holograms can be distinguished by being dark for the initial hologram, while objects from the hologram used for normalization are inverted and appear bright. This is illustrated by figures 4 and 5. However, as increasing the particle number also means an increase in the number of diffraction patterns of out-of-focus particles acting as noise in particle detection algorithms, care has to be taken that this method is only used for low particle number densities; also, the contrast in the inverted hologram is changed, and it seems advisable to avoid considerable overlap of diffraction patterns from the different holograms. Therefore combining two holograms containing diffraction patterns from different particles has to be done with some caution.

The convolution function is sometimes approximated by the Fraunhofer or Fresnel approximation [13, 29, 30], to save one Fourier transform during reconstruction. In our case, however, no approximation is used.

Each pixel of the hologram is subdivided into four sub-pixels for the final reconstructions to avoid artefacts caused by an undersampling of the convolution function³. The sub-pixels measure $3.35 \times 3.35 \mu\text{m}^2$, where each of the sub-pixels has the same bit value as the initial pixel.

The smallest object size that can be reconstructed can be calculated by taking the size of the imaging chip as the size of the aperture that diffracts the reconstructing reference wave field. According to the Rayleigh criterion, the resolution $\delta_{x/y}$ along the x -/ y -axis is then given by [26, 30] $\delta_{x/y} = z \cdot \lambda / L_{x/y}$, where z is the distance between chip and object, λ is the wavelength of the light used, and $L_{x/y}$ is the size of the chip along the x -/ y -axis. The resolution therefore is not constant but depends on the distance between chip and

³ A detailed treatment of this topic is beyond the scope of this paper and will be published elsewhere.

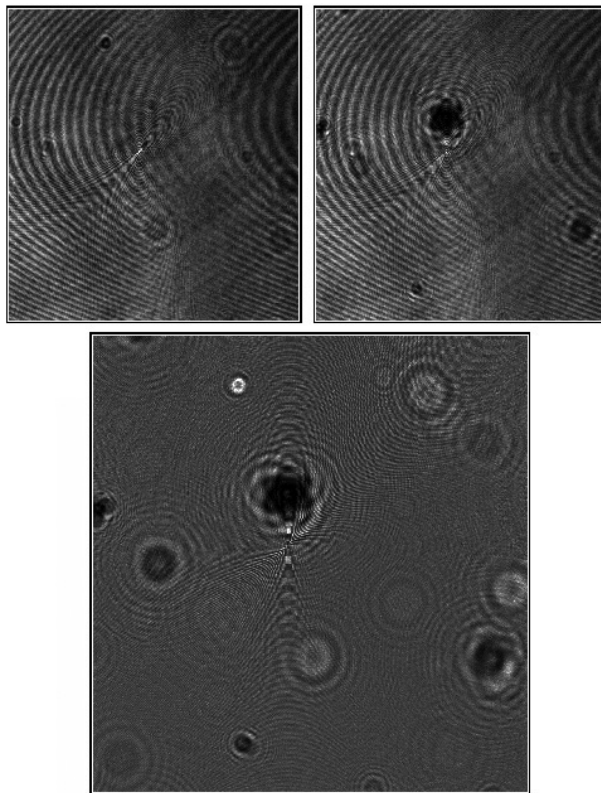


Figure 4. The normalization procedure. The top two images show full views of images taken by the camera in tower T_2 . Dividing the top right image by the top left image yields the normalized hologram as shown below. The normalized hologram shows a smoother background compared to the original images. Diffraction patterns from the top left image are inverted and can thus be distinguished from those from the other original image. The field of view for all images is $6.86 \text{ mm} \times 6.86 \text{ mm}$. A reconstructed image plane of this hologram is shown in figure 5.

object. The minimum resolution, i.e. the coarsest resolution, corresponds to the largest possible distance between imaging chip and object. In our set-up this yields minimum resolutions of roughly $11 \mu\text{m}$ for the camera in tower T_1 and roughly $14 \mu\text{m}$ for the camera in tower T_2 .

The collimation of the beam was calibrated after set-up using a micron-scale brought into the beam path. The beam was found to be slightly divergent, leading to a magnification of about 4% over a distance of 0.1693 m .

The magnification m of an object imaged with diverging light is given by $m(z) = 1/(1 - \frac{z}{z_0})$, where z_0 is the point source origin of the diverging light [11]. Taking $z = 0.1693 \text{ m}$ and $m = 1.04$, we get a virtual point source at $z_0 = 4.402 \text{ m}$. This z_0 was used to determine the magnification $m(z)$ for each reconstructed plane. All particle dimensions given in this article take the respective magnification into account.

Currently, the correct reconstruction distance is determined by applying an iterative procedure with progressively smaller steps in reconstruction distance in combination with a visual sharpness criterion. We estimate the maximum achievable accuracy in determining the depth position for our set-up to be on the order of $\pm 100 \mu\text{m}$.

Examples of holograms and their normalization and reconstruction are shown in figures 4–9.

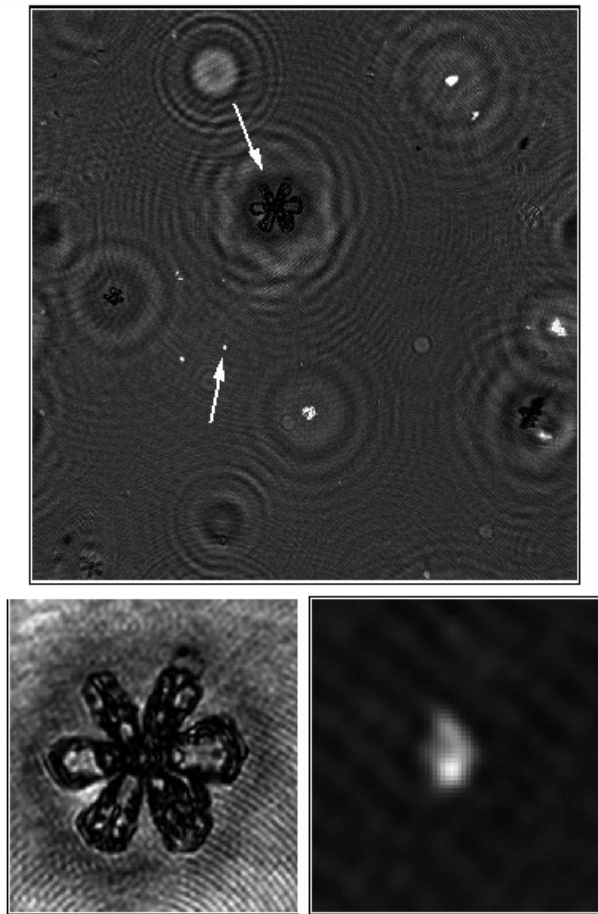


Figure 5. Reconstruction from the normalized holograms. The top image shows a reconstruction of the normalized hologram shown in figure 4, where the reconstruction distance z has been selected to be 176.2 mm. The bottom images show zoomed-in parts of this reconstruction, marked by arrows in the top image. The 2D-distance between the tips of the horizontal branches of the ice crystal on the bottom left picture is roughly $670\ \mu\text{m}$; the width of the bottom left branch at its broad end is roughly $175\ \mu\text{m}$, the width of the ridge in its middle is about $25\ \mu\text{m}$. The particle on the bottom right picture was imaged on the hologram used for normalization, hence it shows up white; its height is about $70\ \mu\text{m}$, its maximum width is about $60\ \mu\text{m}$. The circular diffraction patterns visible in the reconstructed plane are caused by particles at distances different from 176 mm. The field of view of the bottom left image is $1\ \text{mm} \times 1\ \text{mm}$, the field of view of the bottom right image is $235\ \mu\text{m} \times 235\ \mu\text{m}$.

4.1.1. Comparison to other instruments and set-ups. There have been other approaches to solve the depth-of-focus problem using different views of a test volume [15, 17, 23], and to apply digital holography to atmospheric sciences [19, 29]. While a detailed and comprehensive treatment is beyond the scope of this paper, a short and purely qualitative comparison to some related instruments and set-ups may be instructive.

The authors of [15] describe an analogue holographic laboratory set-up aimed at determining the positions of tracer particles in a fluid. In that set-up two laser beams from a pulsed high-power ruby laser intersect at right angles and each beam illuminates a separate holographic film. The general optical configuration is similar in spirit to the configuration used in our instrument. Aimed at performing analogue holography,

the system requires a high power laser system and seemingly special care has to be taken to ensure a repeatable positioning of the film plates, while the system described in this article requires smaller light intensities and does not require any movement of the light recording device for image processing. However, the fact that the set-up described in [15] is used in a laboratory environment alleviates the special demands for analogue holography.

The authors of [17, 23] present a digital holographic system gaining different views of a test volume but using only a single camera. This is achieved by folding the beam path using mirrors such that the beam traverses the test volume several times under different angles before illuminating the camera sensor. This has the advantage that only a single camera is needed, reducing the amount of data to be read out and stored. However, as the beam traverses the volume several times, this method is only suitable for very low particle number densities to avoid loss of coherence and too strong a reduction of the unscattered reference light. Also, this set-up implies that in each view of the particle it has a successively larger distance to the image plane upon reconstruction, which may lead to a considerable loss of resolution between different views, while our set-up allows us to gain views at mutually similar distances.

The authors of [19] and of [29] present single-beam, airborne digital holographic instruments intended for imaging of atmospheric particles. These instruments allow for a single two-dimensional view of particles with the implications for the determination of position and size discussed earlier. In [29] a blur in the reconstructions of large, i.e. millimetre-sized objects is described, where the distances to the plane of the hologram are between 5.4 and 7.3 cm. As possible causes a disturbing presence of the virtual image or a severe occlusion of the unscattered light reaching the imaging chip by the large objects are suggested, where a blur caused by the virtual image would represent a fundamental problem in the short-distance reconstruction of large particles. In figure 6, reconstructions of crystals of similar size are shown. As the crystal in the left column is reconstructed at an even smaller distance than those reported in [29], the blur by the virtual image would be expected to be even more pronounced. However, although the virtual image is visible as a kind of ‘halo’, no considerable blur of the reconstruction is found to be present. To test if a smaller size of the sensor leads to a blur, the hologram has been artificially narrowed down to a size comparable to that of the CCD sensor used in [29]. This is done by eliminating all information contained outside this area by setting the respective values of the hologram to a constant value of 1.0. This ‘narrowed down’ hologram and the reconstruction are shown in figure 7. Also here the reconstruction is not subject to a blur. It therefore seems likely that the blur is also not caused by an occlusion of the unscattered light. However, a difference to our measurements is that those described in [29] were performed with slightly longer laser pulses of 20 ns and at higher airspeeds ($100\ \text{m s}^{-1}$). The observed blur therefore may indicate that despite the short pulse length the particles moved too much during exposure. This would imply that the generally applied rule of thumb, which considers a movement of a particle during exposure of one-tenth of its diameter as acceptable, needs to be modified for non-spherical particles.

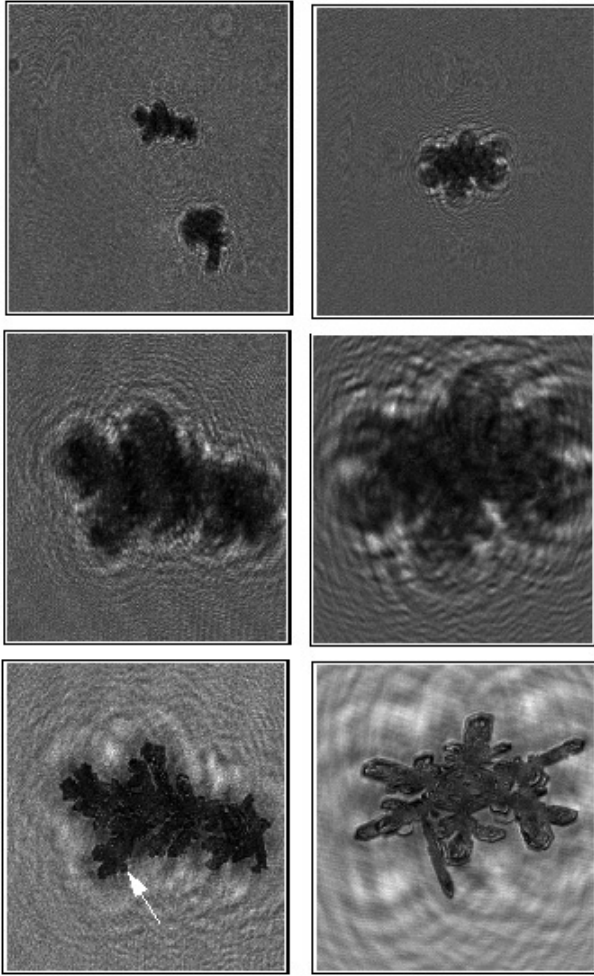


Figure 6. Reconstructions of large objects. The left column shows, from top to bottom, a full view of a hologram normalized as described in the text, a zoomed view of a part of the hologram and a zoomed view of the same part of the reconstructed image. The field of view for the bottom two pictures in the left column is $2.01 \text{ mm} \times 2.01 \text{ mm}$; the reconstruction distance is 4.16 cm . The maximum extension of the crystal in the x -direction is about 1.5 mm ; the maximum extension in y -direction is about 0.9 mm . The crystal seems to have experienced riming as indicated by an uneven surface; the size of the ‘appendix’ marked by the white arrow is about $75 \mu\text{m}$. The right column shows, also from top to bottom, another normalized hologram, a zoomed in part of the hologram and the corresponding part of the reconstructed image. The field of view for the bottom two pictures in the right column is $2.345 \text{ mm} \times 2.345 \text{ mm}$; the reconstruction distance is 15.04 cm . The maximum extension of this ice crystal in the x -direction is about 1.82 mm ; the maximum extension in the y -direction is about 1.36 mm .

4.2. Images in the crossed-beam view

Interpreting images in the crossed-beam view requires some considerations prior to relating the two views to each other. As stated above, the images are taken by cameras not only being in housings standing at an angle of 90° towards each other, but also they are tilted by 45° towards the lid (figure 3). To relate points in the respective views of the two cameras, we need to transform the coordinates (x_1, y_1, z_1) of a point in the image taken by the camera in tower T_1 into the corresponding coordinates (x_2, y_2, z_2) as seen by the other camera, where the

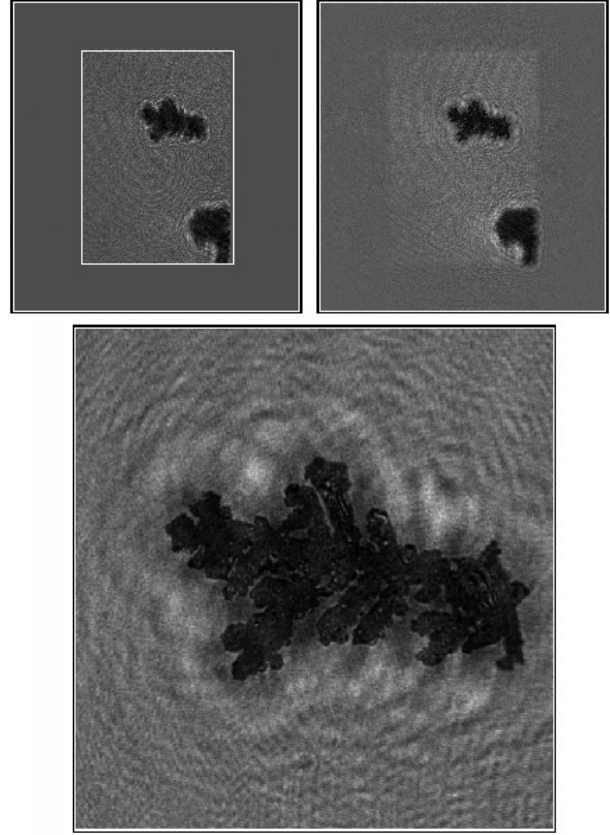


Figure 7. Simulating a reconstruction from a smaller hologram. The top left image shows a modified version of the hologram from figure 6. To simulate a sensor size comparable to that in [29], only the central piece of the original hologram comparable in size is used; the remaining area of the hologram is set to a constant value. Here, this central area is additionally marked by a white rectangle. The top right image shows a complete view of the reconstructed hologram; the bottom image shows a zoomed in part of this reconstruction. The part of the reconstruction of this artificially narrowed down hologram shown in the bottom image corresponds to the bottom left image in figure 6.

distance of the point from the origin is L . Transforming the coordinates of one image into those of the other requires the following steps (see also figure 3):

- (i) Turn the coordinate system by an angle $\gamma = 45^\circ$ about the x -axis.
- (ii) Turn it by an angle $\theta = 90^\circ$ about the y -axis.
- (iii) Turn it back by $-\gamma = -45^\circ$ about the x -axis.

This is best done by multiplying three matrices describing the rotation about x - and y -axes, respectively.

Similar to the arrangement above, let a coordinate system denoted by an index 2 be such that its x_2, y_2 -plane is parallel to that of the camera in tower T_2 , and furthermore let a system denoted by an index 1 have its x_1, y_1 -plane parallel to that of the camera in tower T_1 . This yields the following relation:

$$\begin{pmatrix} x_2 \\ y_2 \\ z_2 \end{pmatrix} = \begin{pmatrix} 1 & 0 & 0 \\ 0 & \cos \gamma & \sin \gamma \\ 0 & -\sin \gamma & \cos \gamma \end{pmatrix} \begin{pmatrix} \cos \theta & 0 & -\sin \theta \\ 0 & 1 & 0 \\ \sin \theta & 0 & \cos \theta \end{pmatrix} \times \begin{pmatrix} 1 & 0 & 0 \\ 0 & \cos \gamma & -\sin \gamma \\ 0 & \sin \gamma & \cos \gamma \end{pmatrix} \begin{pmatrix} x_1 \\ y_1 \\ z_1 \end{pmatrix}$$

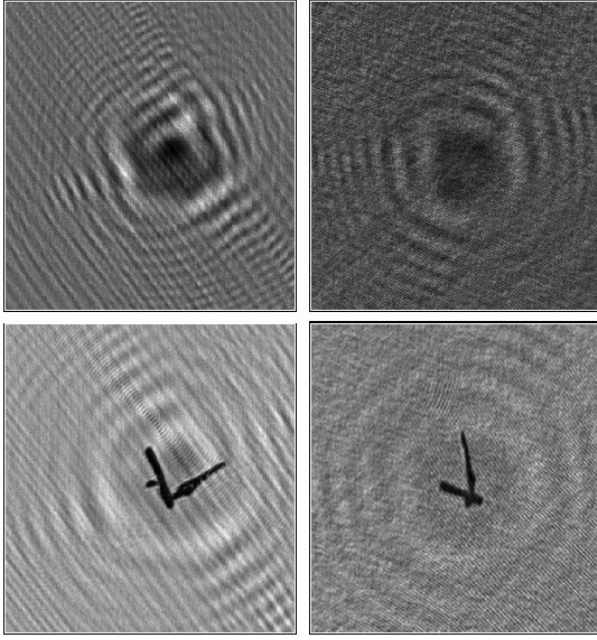


Figure 8. A cross-view. Shown is a currently unidentified object imaged in the cross volume, where the two laser beam paths intersect. The top row shows the normalized diffraction images, where the left image was taken by the camera in tower T_1 , the right image by the camera in tower T_2 . The bottom row shows the corresponding numerical reconstructions, where the right image is reconstructed at a distance $z = 148.6$ mm, the left image at a distance of 104.1 mm. The field of view of the parts of the images shown is 2.01 mm \times 2.01 mm.

$$= \begin{pmatrix} \cos \theta & -\sin \theta \sin \gamma \\ \sin \theta \sin \gamma & \cos^2 \gamma + \cos \theta \sin^2 \gamma \\ \sin \theta \cos \gamma & -\sin \gamma \cos \gamma + \cos \theta \sin \gamma \cos \gamma \\ & -\sin \theta \cos \gamma \\ & -\cos \gamma \sin \gamma + \cos \theta \cos \gamma \sin \gamma \\ & \sin^2 \gamma + \cos \theta \cos^2 \gamma \end{pmatrix} \times \begin{pmatrix} x_1 \\ y_1 \\ z_1 \end{pmatrix}.$$

To transform coordinates with index 2 into coordinates with index 1, θ can simply be replaced by $-\theta$, yielding the following relation:

$$\begin{pmatrix} x_1 \\ y_1 \\ z_1 \end{pmatrix} = \begin{pmatrix} \cos \theta & +\sin \theta \sin \gamma \\ -\sin \theta \sin \gamma & \cos^2 \gamma + \cos \theta \sin^2 \gamma \\ -\sin \theta \cos \gamma & -\sin \gamma \cos \gamma + \cos \theta \sin \gamma \cos \gamma \\ & +\sin \theta \cos \gamma \\ & -\cos \gamma \sin \gamma + \cos \theta \cos \gamma \sin \gamma \\ & \sin^2 \gamma + \cos \theta \cos^2 \gamma \end{pmatrix} \times \begin{pmatrix} x_2 \\ y_2 \\ z_2 \end{pmatrix}.$$

From these equations, the following relations for z_1 and z_2 follow:

$$\begin{aligned} z_1 &= -1/(\sin \theta \cos \gamma)x_2 + [(\cos \theta)/(\cos \gamma \sin \theta)]x_1 \\ &\quad - [(\sin \gamma)/\cos \gamma]y_1, \\ z_2 &= +1/(\sin \theta \cos \gamma)x_1 - [(\cos \theta)/(\cos \gamma \sin \theta)]x_2 \\ &\quad - [(\sin \gamma)/\cos \gamma]y_2. \end{aligned}$$

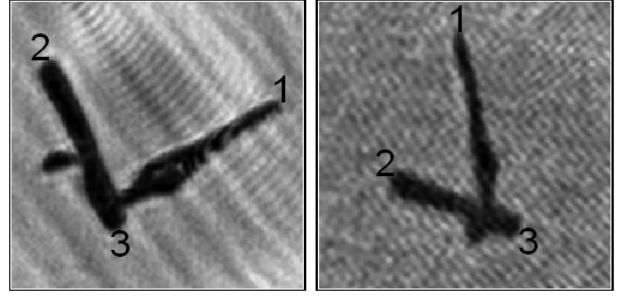


Figure 9. Interpreting cross-view images. The images are zoomed-in versions of the bottom row of figure 8, where the points discussed in the text are numbered. The field of view for both images is 670 μ m \times 670 μ m.

Having calculated z_1 and z_2 , we can compute the distances $L_1 = (x_1^2 + y_1^2 + z_1^2)^{\frac{1}{2}}$ and $L_2 = (x_2^2 + y_2^2 + z_2^2)^{\frac{1}{2}}$ in the images. As distances are not changed by rotations of the coordinate system, L_1 and L_2 should ideally be the same, $L_1 = L_2 = L$; however, small deviations are expected to occur due to uncertainties in the angles and in determining the positions in the image. Nevertheless, computing a distance in both systems can serve as a cross-check to make sure that identical points were identified in both views and that the angles were chosen correctly.

To illustrate this procedure, the reconstructions of the object shown in figure 8 are discussed as an example. Figure 9 shows a zoom-in of the cross-view of the currently unidentified object, imaged on 28 February at 9.33 am local time. Here we calculate the distances $\overline{12}$, $\overline{13}$, and $\overline{23}$ indicated in figure 9.

First, we note that for our set-up $\gamma = 45^\circ$ and $\theta = 90^\circ$, i.e. $\sin \gamma = \cos \gamma = 1/(\sqrt{2})$, $\cos \theta = 0$, and $\sin \theta = 1$. This simplifies the relations for z_1 and z_2 , and they become

$$z_1 = -y_1 - \sqrt{2}x_2,$$

$$z_2 = -y_2 + \sqrt{2}x_1.$$

The origin of the coordinate system is chosen to be at point 1, i.e. on the tip of the curved branch of the object for distances $\overline{12}$ and $\overline{13}$, and at point 2 for distance $\overline{23}$. The magnifications due to the divergence of the laser beam are 1.024 for the left image and 1.035 for the right image; these are corrected for. The resulting distances are given in table 1.

It can be seen that L_1 and L_2 partially agree very well as expected. However, the larger deviation for distance $\overline{23}$ illustrates the difficulty of finding exactly corresponding points and indicates that the angles in the set-up are probably not exactly 45° and 90° . When setting e.g. $\theta = 85^\circ$, the differences in distances become smaller for all three distances $\overline{12}$, $\overline{13}$, and $\overline{23}$, where the difference in $\overline{23}$ reduces to 21 μ m (406 μ m versus 427 μ m). As the current set-up could be aligned rather coarsely only, this is not too surprising and stresses the importance of having more precisely defined angles. However, the good agreement in the separate determinations of distances $\overline{12}$ and $\overline{13}$ indicates that this method is well suited for precise distance determinations under appropriate conditions. Errors will mainly be introduced by external factors, such as uncertainties in identifying corresponding points in the

Table 1. The coordinates of points 2 and 3 in figure 9 with respect to point 1 (and 2), and the corresponding distances. The coordinates in columns 2-7 represent the distances in the first column as two-dimensional vectors in relative coordinates, relative to the position of point 1 in the case of $\overline{12}$ and $\overline{13}$, and relative to that of point 2 in the case of $\overline{23}$. They are given in pixel units, where 1 pixel = $3.35 \mu\text{m}$. The last column gives the geometric mean $L_{\text{gm}} = (L_1 + L_2)/2$ of the corresponding distances L_1 and L_2 . Values with an index m do not take the magnifications of 1.024 and 1.035 in the respective image planes into account. Values given in microns are rounded to the next integer. The values are given for $\gamma = 45^\circ$ and $\theta = 90^\circ$.

	$(x_1, y_1)_m$	$(x_2, y_2)_m$	(x_1, y_1)	(x_2, y_2)	L_1	L_2	$L_{\text{gm}} (\mu\text{m})$
$\overline{12}$	$(-158, 29)_m$	$(-45, -97)_m$	$(-154, 28)$	$(-44, -94)$	160.2 (537 μm)	161.5 (541 μm)	(539 ± 2)
$\overline{13}$	$(-111, -86)_m$	$(41, -133)_m$	$(-108, -84)$	$(40, -129)$	139.5 (467 μm)	137.2 (460 μm)	(464 ± 4)
$\overline{23}$	$(47, -115)_m$	$(86, -36)_m$	$(46, -112)$	$(83, -35)$	121.2 (406 μm)	134.6 (451 μm)	(429 ± 23)

two views, a missing optical calibration or, as in our case, uncertainties in the angles.

We estimate that for this dataset we can determine 3D distances to an accuracy of $\pm 25 \mu\text{m}$, being limited mainly by instrumental uncertainties with room for improvement. Already this accuracy is, at least for large objects such as the object shown in figure 9, much better than what is achieved by determining 3D distances by determining the z -position where the object is in focus.

It is also interesting to note that judging e.g. from the right image in figure 9 only, as would be the case in a single-beam non-holographic imaging device if the particle were in focus [19, 29], the distances would have been underestimated by up to 35%. This is because distance $\overline{12}$ makes an angle of about 50° with respect to the (x_2, y_2) -plane, which does not even represent a worst case scenario.

4.2.1. Calculating the volume—an example. To give a general idea of how volume and surface area of a particle may be estimated from the double image, and to illustrate the limitations, a short example is given.

The object shown in figure 9 consists of several branches; here, the branch labelled $\overline{23}$ is used to give an example. If we assume that the cross-section of the segment $\overline{23}$ perpendicular to the direction of $\overline{23}$ in the image plane is circular, its volume can be estimated according to the following procedure.

- (i) Subdivide the segment into pieces with a height of Δh (measured along the direction of $\overline{23}$ in the image plane).
- (ii) Determine the width r of the segment perpendicular to Δh .
- (iii) Calculate the volume V_c of the cylinder with height Δh and radius r .
- (iv) Add up the volumes of the small cylinders to get the total volume V' .
- (v) To get the final volume V , multiply V' with $1/m^3$, where m is the magnification, and with the ratio $L_{\text{gm}}/L_{2\text{dim}}$, where $L_{2\text{dim}}$ is the apparent length of $\overline{23}$ in the image plane, while L_{gm} is the true length in three-dimensional space, both corrected for the magnification.
- (vi) The procedure can be repeated with the second view of the segment.

Prior to applying this procedure, the image is transformed into a binary image as illustrated in figure 10. To this end, pixels in those parts of the object which will not be considered are assigned a value in the range of the background values. Next, for binarization a value of 1 is assigned to all pixels with a value above a certain threshold, while a value of 0 is assigned

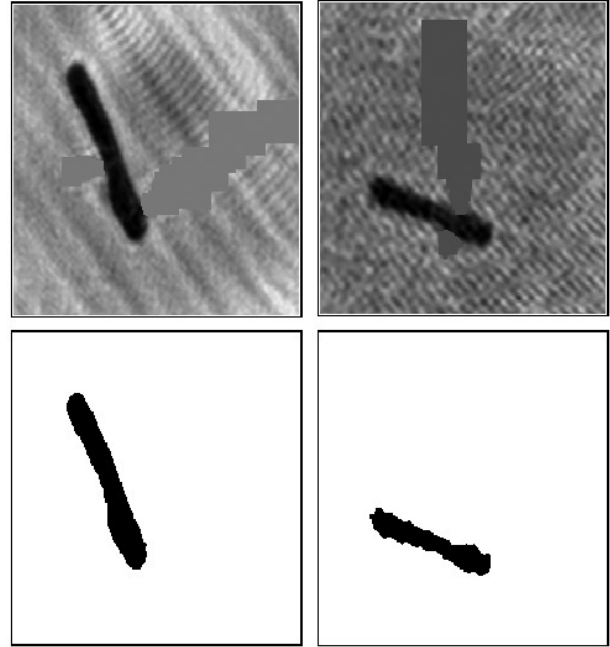


Figure 10. Segmentation and binarizing. The figure illustrates how a segment from the object shown in figure 9 is selected and the image is transformed into a binary image using a threshold value as described in the text.

to the other pixels. The threshold is chosen such that pixels belonging to the image of the particle have values which do not exceed the threshold value. As the background is not uniform, pixels clearly not belonging to the object image may also have values below the threshold. They are set to 1 manually before determining the object area.

The threshold here was chosen manually judging by visual criteria. As it was found that a range of thresholds seemed acceptable, the procedure described above was performed twice for each view, once for a maximum value of the threshold and once for a minimum value, where these values were different for the different views.

This procedure yields estimates of the volume of:

$$V_1 = (1.47 \pm 0.15)\text{nl}, \quad \text{and}$$

$$V_2 = (1.05 \pm 0.21)\text{nl},$$

where an index 1 (2) corresponds to the view in the left (right) image in figure 9 and the error margins have been calculated as

maximum errors based on the maximum/minimum values of V' and L_{gm} ; 1 nl corresponds to 10^{-12} m³.

According to the method of subdivision into circular cylinders with a height Δh and a radius r_i , the surface area S may be estimated as $S = 2\pi \cdot \Delta h \sum_{i=0}^{i=i_{\text{max}}} r_i + \pi r_0^2 + \pi r_{i_{\text{max}}}^2 + \pi \sum_{i=1}^{i=i_{\text{max}}} (r_i^2 - r_{i-1}^2)$. For the case considered above, without taking into respect the fact that part of the surface area is covered by the other segments, this yields values for the surface area of $S_1 = (1.80 \times 10^{-7} \pm 0.24 \times 10^{-7})$ m² and $S_2 = (1.36 \times 10^{-7} \pm 0.14 \times 10^{-7})$ m².

The result for the volume and the surface area illustrates certain features and limitations of the technique. While it can be said that e.g. the volume of branch $\overline{23}$ is on the order of 1 nl, the absolute values for the volume calculated from the different views are not consistent within the error margins under the assumption of a circular cross-section. This may reflect the fact that even for perfectly circular cross-sections the difference in the angle of projection may lead to different results in the sense that e.g. an estimate based on the view of $\overline{23}$ in the left image of figure 9 would reveal more details of the shape than that based on the right image. The deviation in the results may also be caused by an underestimate of the error margins of the quantities used for the calculation of the volume, or the assumption of a circular cross-section perpendicular to $\overline{23}$ does not hold. However, if the error margins are correct, for example, the ratio of the average radii for the respective views may be used to model other, non-circular cross-sections, representing e.g. an upper or lower bound of the volume.

The limitations of calculating the volume of an object from two views are quite obvious: for highly irregularly shaped objects consisting of many segments with different orientations which overlap in the projections, the process of segmentation will become difficult. Accordingly, the error in the estimate of the volume will be rather large. For simple objects on the other hand, like columns of hexagonal plates, or for regularly shaped or coplanar objects such as rather regular, star-like ice crystals, the method seems to be suited to improve the accuracy of volume estimates.

Calculations of the surface area, however, based on ideal three-dimensional bodies like cylinders, will only represent a lower bound and may be a gross underestimate, unless the microscopic roughness of the surface beyond the resolution limit is known.

5. Summary and outlook

In this paper, an outdoor ground-based digital-holographic system for *in situ* imaging of atmospheric ice particles was presented, which has the possibility to use a crossed-beam inline digital-holographic set-up. Additionally, we presented initial results from its first deployment at the High Altitude Research Station Jungfraujoch.

The light source was a pulsed nanosecond laser; the imaging system consisted of two 1.3 MPixel CMOS-cameras. We were able to obtain clear images of large atmospheric ice crystals at distances ranging from around 4 cm to around 17.5 cm. By using a crossed-beam set-up, we were able to considerably improve the determination of three-dimensional shape and position of particles in the cross volume, as compared to a single-beam set-up. We have shown how

distances in three-dimensional space can be inferred from the two views of objects in the cross volume, where we currently achieve an accuracy of at least ± 25 μm . An example of a method to estimate the volume and a lower bound of the surface area of objects imaged in the cross-view has been given.

Apart from obvious improvements such as enhancing the stability of the optical components, it is intended to change the instrument in such a way that the optics are also accessible more easily after initial installation and can be aligned more precisely with better defined angles.

A necessary change will be to improve the camera towers' design with respect to aerodynamics to minimize distortion of the airflow, which currently is expected to lead to an undersampling of large objects, especially at low wind-speeds. With respect to the optical system, a straightforward change would be to replace the current imaging chips by larger chips, to improve image resolution and to make the total observed volume larger as well as the cross volume. However, as this means that each image would need more disk space and more computational power for reconstruction, and as the larger image size would infringe upon the maximum possible frame rate it depends upon the desired performance of the system whether or not such a change would be an improvement. The same is true for the angle of intersection of the crossed beams. For e.g. a ground-based measurement of falling raindrops the special case of a 90° crossed-beam set-up, where $z_1 = -x_2$ and $z_2 = x_1$ as in analogue laboratory set-ups for investigations of fluids [15, 28], may be regarded as favourable. Also, under different environmental conditions it might be necessary to cool the instrument instead of heating it. For these reasons, it is planned to further increase the modularity of the instrument, in the sense that, without much hassle, the instrument can be 'switched' between different set-ups, to be able to choose the most favourable set-up for a given environmental situation.

In the future it is intended to carry out automated image analysis to obtain total particle number, inter-particle distances, particle sizes and volumes.

Acknowledgments

We would like to thank S Mitra, K Diehl and I Hoog for giving us the opportunity to test the instrument in the Mainz walk-in cold chamber. We thank the staff of the mechanical and electronics workshops of the Institute for Atmospheric Physics and of the mechanical workshop of the Max-Planck-Institute for Chemistry. In particular, we would like to thank E Leistler for her helpfulness and commitment, and T Böttger for his help by designing a storm-proof mounting of the instrument. We would also like to thank T Moll from CryLas, as well as the staff from Basler for technical support and their flexibility and kindness when quick solutions were required. We are grateful to MeteoSwiss for making meteorological data available to us, and in particular to the 'International Foundation High Altitude Research Stations Jungfraujoch and Gornergrat' for giving us the opportunity to perform a field-campaign at the Jungfraujoch, where the staff of the research station did their utmost to ensure a successful campaign. We also thank the anonymous reviewers for detailed and helpful comments.

We gratefully acknowledge funding of this work, which is part of the PhD thesis of SMFR, by the *Deutsche Forschungsgemeinschaft (DFG)* as part of the collaborative research centre *Die troposphärische Eisphase (SFB641)*.

References

- [1] Gabor D 1948 *Nature* **161** 777
- [2] Silverman B A, Thompson B J and Ward J H 1964 *J. Appl. Meteorol.* **3** 792
- [3] Thompson B J, Parrent G B, Ward J H and Justh B 1966 *J. Appl. Meteorol.* **5** 343
- [4] Thompson B J, Ward J H and Zinky W R 1967 *Appl. Opt.* **6** 519
- [5] Goodman J W and Lawrence R W 1967 *Appl. Phys. Lett.* **11** 77
- [6] Pavitt K W, Jackson M C, Adams R J and Bartlett J T 1970 *J. Phys. E: Sci. Instrum.* **3** 971
- [7] Collier R J, Burckhardt C B and Lin L H 1971 *Optical Holography* (New York: Academic) p 334
- [8] Bexon R, Gibbs J and Bishop G D 1976 *J. Aerosol Sci.* **7** 397
- [9] Conway B J, Caughey S J, Bentley A N and Turton J D 1982 *Atmos. Environ.* **16** 1193
- [10] Brown P R A 1989 *J. Atmos. Ocean. Technol.* **6** 293
- [11] Vikram C S 1992 *Particle Field Holography* (Cambridge: Press Syndicate of the University of Cambridge) p 23, eq. 3.18; note that for our case: $n = 1$, $z_c = \infty$
- [12] Borrmann S and Jaenicke R 1993 *J. Atmos. Ocean. Technol.* **10** 277
- [13] Schnars U and Jüptner W 1994 *Appl. Opt.* **33** 179
- [14] Lawson R P and Cormack R H 1995 *Atmos. Res.* **35** 315
- [15] Zhang J, Tao B and Katz J 1997 *Exp. Fluids* **23** 373
- [16] Liu F and Hussain F 1998 *Opt. Lett.* **23** 132
- [17] Adams M, Kreis T M and Jüptner W P O 1997 *Proc. SPIE* **3098** 234
- [18] Uhlig E M, Borrmann S and Jaenicke R 1998 *Tellus B* **50** 377
- [19] Lawson R P, Korolev A V, Cober S G, Huang T, Strapp J W and Isaac G A 1998 *Atmos. Res.* **47/48** 181
- [20] Vössing H J, Borrmann S and Jaenicke R 1998 *Atmos. Res.* **49** 199
- [21] Korolev A V, Strapp J W and Isaac G A 1998 *J. Atmos. Ocean. Technol.* **15** 708
- [22] Feigl C, Schlager H, Ziereis H, Curtius J, Arnold F and Schiller C 1999 *Geophys. Res. Lett.* **26** 2215
- [23] Kebbel V, Adams M, Hartmann H J and Jüptner W 1999 *Meas. Sci. Technol.* **10** 893
- [24] Bronstein I N, Semendjajew K A, Musiol G and Mühlhig H 1999 *Taschenbuch der Mathematik* 4th edn (Frankfurt/Main: Verlag Harri Deutsch) p 727
- [25] Borrmann S, Luo B and Mishchenko M 2000 *J. Aerosol Sci.* **31** 789
- [26] Hecht E 2001 *Optik* 3rd edn (München/Wien: Oldenbourg Verlag) p 682
- [27] Kondo Y *et al* 2003 *Geophys. Res. Lett.* **30** 1154
- [28] Sheng J, Malkiel E and Katz J 2003 *Appl. Opt.* **42** 235
- [29] Fugal J P, Shaw R A, Saw E W and Sergeev A V 2004 *Appl. Opt.* **43** 5987
- [30] Schnars U and Jüptner W 2005 *Digital Holography* (Berlin: Springer)
- [31] Voigt C, Schlager H, Ziereis H, Kärcher B, Luo B P, Schiller C, Krämer M, Popp P J, Irie H and Kondo Y 2006 *Geophys. Res. Lett.* **33** L05803